

# Searching for ultralight axions with twisted cavity resonators of anyon rotational symmetry with bulk modes of nonzero helicity

J. F. Bourhill, E. C. I. Paterson<sup>✉</sup>, M. Goryachev, and M. E. Tobar<sup>✉</sup>

*Quantum Technologies and Dark Matter Labs, Department of Physics, University of Western Australia,  
35 Stirling Highway, 6009 Crawley, Western Australia*



(Received 28 August 2022; revised 19 May 2023; accepted 11 September 2023; published 29 September 2023)

Möbius-ring resonators stem from a well-studied and fascinating geometrical structure which features a one-sided topology, the Möbius strip, and have been shown to exhibit fermion rotational symmetry with respect to a ring resonator with no twist (which exhibits boson rotational symmetry) [Phys. Rev. Lett. **101**, 247701 (2008)]. Here, we present a new type of resonator through the formation of twisted hollow structures using equilateral triangular cross sections, which leads to the realization of a cavity with anyon rotational symmetry. Unlike all previous cavity resonators, the anyon resonator permits the existence of bulk resonant modes that exhibit nonzero electromagnetic helicity in vacuo, with nonzero overlap of the electric and magnetic mode eigenvectors,  $\int \mathbf{E}_p \cdot \mathbf{B}_p d\tau$ , integrated over the cavity volume. In the upconversion limit, we show that these nonzero helical modes couple naturally to ultralight dark matter axions within the bandwidth of the resonator by adding amplitude modulated sidebands through the axion-photon chiral anomaly. Thus, we show a sensitive ultralight dark matter experiment may be realized by implementing such a resonator in an ultrastable oscillator configuration and searching for signals in the Fourier spectrum of amplitude fluctuations. This removes the typical requirement for an external magnetic field and therefore permits the use of superconducting materials to reduce surface losses and enhance sensitivity to axions.

DOI: [10.1103/PhysRevD.108.052014](https://doi.org/10.1103/PhysRevD.108.052014)

## I. INTRODUCTION

Chirality is a fundamental property present in many physical systems, which exhibit asymmetry, ranging from particle physics [1–3], topological and quantum systems [4–10], complex molecules, and chiroptical phenomena [11–16]. Many of these occur as surface states, at high energy or frequency, or due to complex meta-structures [17–19] or plasmonic systems [20,21], which inevitably add loss. Here, we realise a new class of electromagnetic resonator, which we call the “anyon cavity resonator,” based on twisted waveguide and “Möbius-like” structures [22], of twist angle  $\phi$ , which exhibit monochromatic bulk chiral modes at microwave frequencies with nonzero helicity through a photonic magneto-electric coupling in vacuo. We show the modes couple to axion dark matter as amplitude modulations, without the need for a background field, with near unity form factors and in the ultra-light mass range from  $10^{-22}$  to  $10^{-14}$  eV [23–26].

This not only significantly reduces the complexity but also allows the possibility of utilizing low-loss superconducting resonators [27–30] to search for ultralight dark matter (ULDM) axions.

ULDM axions have been shown to solve the standard model strong charge-parity problem [31–34], could account for the entire dark matter of the universe [35–38], and are usually searched for using putative axion interactions with gluons and neutrons [39–42]. These experiments must be maintained for multiple years to search for ULDM, for example a particle mass of  $10^{-22}$  eV corresponds to a frequency of 24.2 nHz with a period of 1.3 years. Upconversion techniques, which utilise two real photon modes with nonzero overlap integral,  $\int \mathbf{E}_n \cdot \mathbf{B}_m d\tau$  can work in a similar way to the ULDM frequency comparison experiments if they are made near degenerate [43–50]. However, feedthrough, mode coupling, nonlinear effects, and injection locking are likely to limit the minimum frequency detuning between two modes, so they are not configurable for ultralight axions. In contrast, the anyon cavity resonator has eigenmodes of nonzero helicity [51–58], where the sign of the helicity depends on whether the modes  $\mathbf{E}$  field and  $\mathbf{B}$  field have net parallel alignment (+ve) or net antiparallel alignment (–ve), and is given by,

Published by the American Physical Society under the terms of the [Creative Commons Attribution 4.0 International](https://creativecommons.org/licenses/by/4.0/) license. Further distribution of this work must maintain attribution to the author(s) and the published article’s title, journal citation, and DOI. Funded by SCOAP<sup>3</sup>.

$$\mathcal{H}_p = \frac{2\text{Im}[\int \mathbf{E}_p(\vec{r}) \cdot \mathbf{B}_p^*(\vec{r}) d\tau]}{\sqrt{\int \mathbf{E}_p(\vec{r}) \cdot \mathbf{E}_p^*(\vec{r}) d\tau \int \mathbf{B}_p(\vec{r}) \cdot \mathbf{B}_p^*(\vec{r}) d\tau}}, \quad (1)$$

In this work we show the square of the magnitude of the helicity,  $|\mathcal{H}_p|^2$ , is equivalent to the form factor that couples low-mass axions to photons as an amplitude modulation of a single mode through a parametric interaction. The normalized helicity in (1) can range between  $\pm 1$  and is tied to the conservation of Zilch [59], or photonic chirality [15] and is usually considered when photons interact with chiral molecules or materials [12,14,15]. Analogously, the axion is calculated to couple to photons through a chiral anomaly, whether in condensed matter physics [6,8] or in quantum chromodynamics (QCD) [31,33,34,60] and the introduction of the axion as a modification to Maxwell's equations in fact introduces a nonzero Zilch to the equations of motion.

## II. TWISTED TRIANGULAR RESONATORS

We investigate two twisted triangular cavity configurations as depicted in Fig. 1: (a) a linear twisted resonator with electrically conducting boundary conditions at the ends, which allows arbitrary twist angle,  $\phi$ , and (b) a twisted ring resonator similar to a Möbius strip, with only discrete allowed  $\phi$  values ( $\phi = \mathbb{Z}\pi/3$ ).

It has been previously demonstrated that a Möbius ring resonator with rectangular cross section and  $\pi$  twist angle exhibits fermion rotational symmetry with respect to the boson rotational symmetry of a ring resonator with no twist angle [22]. This can be understood by considering some 2D function confined to the resonator's cross section; in the ring resonator, the function is invariant under one full cycle of the cavity circumference, while in the Möbius configuration it requires two full cycles. In the triangular ring system depicted in Fig. 1(b) we observe that such a 2D

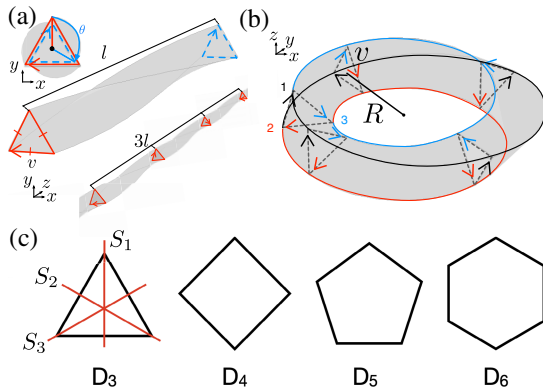


FIG. 1. Geometries considered; (a) the twisted triangular waveguide resonator and (b) the triangular Möbius-like ring resonator. (c) The dihedral group of regular convex polygons,  $D_n$ , which have  $2n$  symmetries;  $n$  rotational and  $n$  reflection.

function confined to the cavity cross section (the arrow head) is invariant after three rotations. Furthermore, considering the linear case of Fig. 1(a), we are free to set the twist angle  $\phi$  to any value, and therefore some 2D function will be invariant after  $2\pi/\phi$  cycles of the cavity (3 lengths are required for invariance in the depicted case). Thus we can state that such systems exhibit anyon rotational symmetry.

### A. Twisted triangular linear resonator

In the linear resonator of Fig. 1(a), by introducing the twist angle  $\phi$  the resonator's mirror symmetry is broken and the resulting geometry is chiral; right handed for  $\phi > 0$  and left handed for  $\phi < 0$ . This geometry dictates the boundary conditions which are used to solve Maxwell's equations for the resonant electromagnetic modes within this volume. The introduced mirror asymmetry of the boundary conditions results in a magnetoelectric coupling [61], which acts to couple the degenerate TE and TM modes of the untwisted cavity together into a new orthogonality basis. This can be alternatively interpreted as a dual transformation [57] of the no-longer orthogonal  $\mathbf{E}$  and  $\mathbf{B}$  fields into a new orthogonality basis  $\mathbf{E}'$  and  $\mathbf{B}'$  which are some combination of the original fields.

The result is that as a function of twist angle, the new eigenmodes of the cavity have some nonzero  $\mathbf{E} \cdot \mathbf{B}$  product and hence  $\mathcal{H}_p$ , and are asymmetrically detuned in opposite directions from their untwisted frequencies. The origin of this mode tuning can be thought of as a normal mode splitting between two coupled harmonic oscillators and the sign of the resulting helicity reflects the phase with which they are coupling. When considering the emergent helicity of the modes when twisted, there are two impacting factors of the cavity cross section—the polygon order and the symmetry. In regards to the former, the equilateral triangle is the lowest order polygon of the dihedral group of regular polygons [see Fig. 1(c)] and as such, least approximates a circle. One can imagine the two resonators depicted in Figs. 1(a) and 1(b) with a circular cross section; they would not appear any different from a cylinder or torus cavity, respectively. Therefore it reasons that the greatest impact of the twisting angle  $\phi$  will be generated by the lowest order regular polygon.

This is further demonstrated in Fig. 2(a) as the greatest magnitude helicity modes in cavities with  $D_3$  to  $D_5$  polygon cross-sections are shown as a function of twist angle. The two  $D_3$  modes (one that tunes up and one that tunes down in frequency) approach near unity helicity, while higher order cross-sections result in smaller values.

The symmetry of the cross section also plays an important role, as a perfectly symmetric cross section (i.e., equilateral triangle, square etc.) results in TE and TM modes being tuned coincident in frequency with one another. Just like any coupled mode system, hybridization

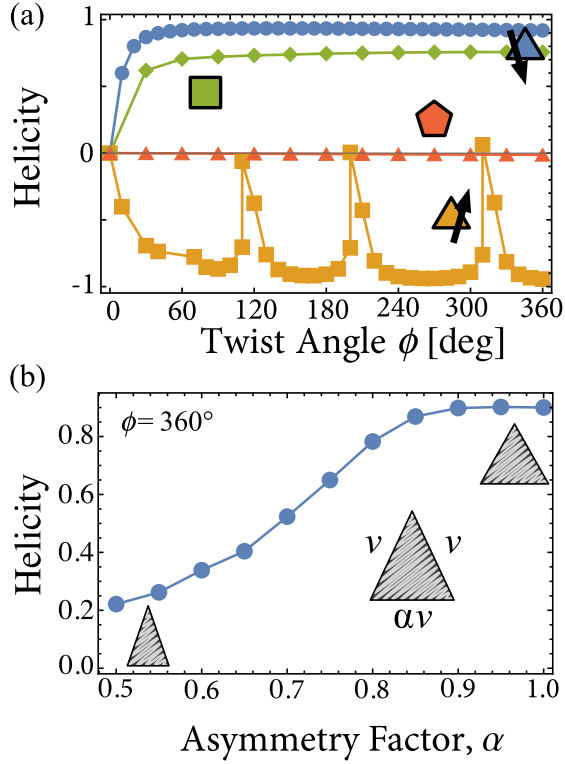


FIG. 2. (a) Calculated  $\mathcal{H}_p$  values as a function of  $\phi$  for right and left handed modes, with equilateral triangular (blue and yellow), square (green) and pentagonal (red) cross section. Modes tuning up in frequency have -ve  $\mathcal{H}_p$  (with spurious mode interactions), while modes tuning down have -ve as indicated by the arrow. (b) Impact of varying the equilateral symmetry of the cross section  $\alpha$  on mode helicities for  $\phi = 360^\circ$ .

of the two individual systems is greatest when their frequencies are made degenerate. This is true for the helicity of the hybrid mode here, as demonstrated by Fig. 2(b), in which one of the vertex lengths is multiplied by some factor  $\alpha$ , and we observe that helicity is maximized for the equilateral case. To confirm the expected frequency splitting in the linear resonator as  $\phi$  is varied, we 3D printed three aluminium prototypes with right handed twist (+ve  $\phi$ ) using selective laser melting, using a similar method to previously reported superconducting cylindrical cavity resonators [27]. These resonators have a length of 150 mm and their cross section has a vertex length of 20 mm. The experimentally obtained transmission spectra are measured at room temperature through coaxial probes placed at the cavity end faces and are plotted in the z-axis of Fig. 3, which sit above the spectra obtained from finite element modeling (FEM). We note exceptional agreement between the frequency locations of the resonant modes and the predicted tuning from the simulations. The lowest order mode with high helicity has a bandwidth of  $\kappa \approx 4.1$  MHz, invariant of  $\phi$ , consistent with a surface resistance of  $R_s \sim 470$  m $\Omega$  at room temperature.

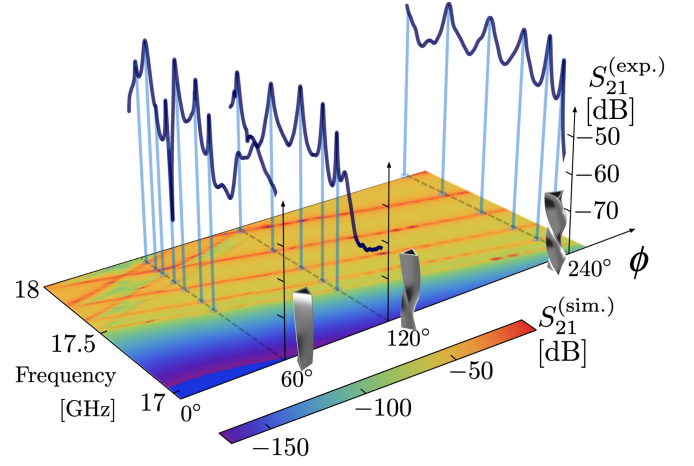


FIG. 3. Experimental transmission measurements,  $S_{21}$ , of the  $60^\circ$ ,  $120^\circ$ , and  $240^\circ$  twisted triangular waveguide cavities (dark blue) overlaying simulated frequency response, shown as the color density plot. Light blue vertical lines indicate the corresponding locations of the resonant transmission peaks of the experimental data.

### B. Twisted triangular ring resonator

Next we consider the case of bending the two end faces of the resonator around and forming a ring as shown in Fig. 1(b); removing two metallic boundaries from the resonator and therefore allowing modes with lower loss. In addition to the resonant frequencies, the electromagnetic helicity and geometry factor [62],  $G_p = Q_{0p}R_s$ , where  $Q_{0p}$  is the unloaded quality factor of the modes, can be obtained from the FEM. The results are presented in Table I for the greatest negative and positive helicity modes, and demonstrate a factor of 3 improvement in  $Q$ -factors for the ring resonator compared to the linear version. However, our attempts to 3D print a ring resonator require two separate parts to be made, which require a knife edge for optimum electrical connectivity, which will need to be considered carefully to attain the predicted  $Q$ -factors.

For comparison, the  $TE_{011}$  mode in a cylindrical resonator has a  $G$ -factor of the order 700 and the  $TM_{010}$  mode is of order 300 [27], so  $Q$ -factors in the anyon cavity resonator, if limited by material surface resistance will have approximately an order of magnitude larger  $Q$ -factors.

TABLE I. Simulated  $f_p$ ,  $G_p$  and  $\mathcal{H}_p$  values for the greatest  $|\mathcal{H}_p|$  modes for the linear and ring resonators with  $l = 150$  mm,  $\nu = 20$  mm,  $\alpha = 1$  and  $\theta = 120^\circ$ .

Resonator	$f_p$ (GHz)	$G_p$ ( $\Omega$ )	$\mathcal{H}_p$
Linear	17.044	1950	-0.931
Linear	17.688	1920	0.8796
Ring	17.022	6200	-0.931
Ring	17.814	7290	0.954

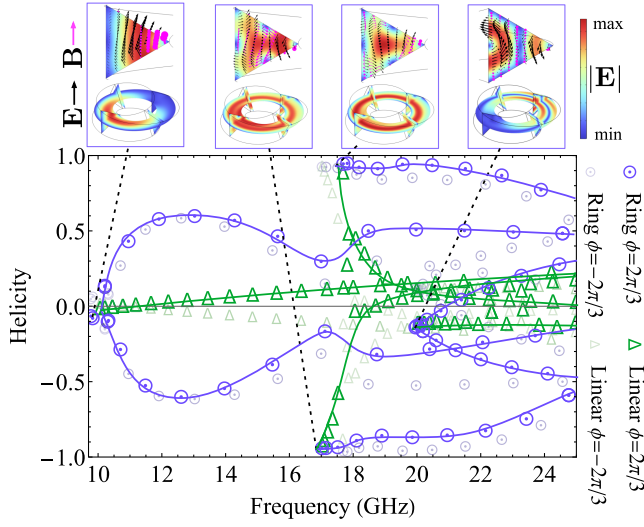


FIG. 4. Simulated  $\mathcal{H}_p$  values for eigenmodes in an equilateral triangular cross-section ring resonator with  $R = 150/2\pi$  mm,  $v = 20$  mm, and  $\theta = 120^\circ$  (purple circles) compared to the same dimension equivalent linear resonator (green triangles). Purple and green lines link modes of a common family. For the first mode of each mode family,  $|\vec{E}|$  is plotted in the inset color density plots and  $\vec{E}$  and  $\vec{B}$  fields as arrows. The opposite twist ( $\phi < 0$ ) data is also plotted, demonstrating a reflection of helicity values in the horizontal axis.

Recent results have shown that an  $R_s$  of 0.63 n $\Omega$  at 1.3 GHz is achievable [28,29], which would result in  $Q$ -factors as high as  $10^{13}$  if the best niobium could be implemented as a ring resonator. The 3D printed aluminium has previously achieved an  $R_s$  of 0.2 m $\Omega$  at 10 GHz at mK temperatures [27], which would mean a  $Q$ -factor of  $10^7$  is initially possible. For axion detection, a lower frequency obtainable with increased area of cross section and volume, and a lower  $R_s$  will enhance the sensitivity.

A comparison of the helicities of the resonant modes in the linear and ring cases are presented in Fig. 4. It can be observed that the greatest  $|\mathcal{H}_p| \sim 1$  modes occur at the same frequency for both resonators, which is the cutoff frequency for the  $TE_{11}$  and  $TM_{11}$  mode families [63,64]. The key difference between the two resonators is seen for this mode branch: it is only the first few modes in the linear case which have large  $|\mathcal{H}_p|$ , while there are numerous high helicity mode candidates in the ring case. This is a result of the lack of end-face boundary conditions permitting both sin and cos azimuthal field dependences in the ring case, one of which is forbidden in the linear case. In the latter, as the number of axial nodes increases, the field overlap between the sin (TE) and cos (TM) modes is largest for the first few modes and then drops, while in the ring, the field overlap integral can be maintained as both sin and cos solutions are permitted for both original polarizations. In both forms of the resonator, the lower frequency modes with cutoff frequency  $\sim 10$  GHz

have no TM counterpart and therefore do not achieve unity  $|\mathcal{H}_p|$ .

### III. AXION MODIFIED ELECTRODYNAMICS

The coupling of axions to photons occurs due to the axion mixing with neutral pions and is thus couples to photons through the chiral anomaly. This “axion-electromagnetic chiral anomaly” may be described by the following interaction term, added to the Lagrangian of the photonic degrees of freedom [65],

$$\mathcal{L}_{a\gamma\gamma} = \frac{g_{a\gamma\gamma}}{4} a F_{\mu\nu} \tilde{F}^{\mu\nu} = g_{a\gamma\gamma} a \vec{E} \cdot \vec{B}. \quad (2)$$

Here, the photonic degrees of freedom are represented by the electromagnetic field tensor strength  $F_{\mu\nu}$  and its dual,  $\tilde{F}^{\mu\nu}$ , while the axion modification to the equations of motion are given by the product of the pseudoscalar,  $a$ , and the photon-axion coupling term  $g_{a\gamma\gamma}$  multiplied by  $\vec{E} \cdot \vec{B}$ .

The photon-axion coupling from Eq. (2) modifies parts of the electrodynamic equations of motion proportionally to the dynamic normalized coupling parameter,  $\Theta(t) = g_{a\gamma\gamma} a(t)$ . Considering the action density for the electromagnetic and axion fields, it has been shown that a set of modified Maxwell’s equations may be written as [66,67],

$$\begin{aligned} \nabla \cdot (\epsilon_0 \vec{E} - \Theta \epsilon_0 c \vec{B}) &= \rho_e \\ \nabla \times \left( \frac{\vec{B}}{\mu_0} + \Theta \frac{\vec{E}}{\mu_0 c} \right) &= \vec{J}_e \\ -\partial_t (\epsilon_0 \vec{E} - \Theta \epsilon_0 c \vec{B}) &= \vec{J}_e \\ \nabla \cdot \vec{B} &= 0 \\ \nabla \times \vec{E} + \partial_t \vec{B} &= 0. \end{aligned} \quad (3)$$

Correspondingly, the axion equation of motion in the nonrelativistic limit leads to a solution of harmonic form, and in the quasistatic limit the local axion field has no spatial dependence, simply given by,

$$\Theta(t) = \theta_0 \cos(\omega_a t) \quad (4)$$

where  $\omega_a = \frac{m_a c^2}{\hbar}$ ,  $\theta_0 = g_{a\gamma\gamma} a_0$  and  $a(t) = a_0 \cos(\omega_a t)$ .

Here we consider cold dark matter in the nonrelativistic limit, where  $a(t)$  is a large classical nonrelativistic pseudoscalar field and  $g_{a\gamma\gamma}$  is an extremely small coupling so  $\theta_0 \ll 1$  and the axion is almost “invisible.”

#### A. Upconversion axion electrodynamics in phasor form and in the rotating wave approximation

For our case the axion Compton frequency,  $\omega_a$ , is smaller than the pumped cavity mode frequency,  $\omega_p$ , ( $\omega_a \ll \omega_p$ ). The axion converts to a weak single tone modulation of the



pump resulting in axion upconversion, creating upper and lower side band at  $\omega_p - \omega_a$  and  $\omega_p + \omega_a$ . The axion pseudo-scalar may be written as,  $\Theta(t) = \frac{1}{2}(\tilde{\theta}e^{-j\omega_a t} + \tilde{\theta}^*e^{j\omega_a t}) = \text{Re}(\tilde{\theta}e^{-j\omega_a t})$ , and in phasor form as,  $\tilde{\Theta} = \tilde{\theta}e^{-j\omega_a t}$ . The phase of the axion is arbitrary, so we set  $\tilde{\theta} = \tilde{\theta}^* = \theta_0$ , related to the root mean square value by,  $\langle \theta_0 \rangle = \frac{\theta_0}{\sqrt{2}}$ .

In contrast, the electric and magnetic fields as well as the electric current are represented as vector-phasors with slowly time varying amplitude and frequency modulations. Here we assume the modulations are single tone monochromatic modulations at the axion frequency,  $\omega_a$ . For example, we set  $\vec{E}(\vec{r}, t) = \frac{1}{2}(\tilde{\mathbf{E}}(\vec{r}, t) + \tilde{\mathbf{E}}^*(\vec{r}, t)) = \text{Re}[\tilde{\mathbf{E}}(\vec{r}, t)]$ . Thus, in the limit that the modulation is weak compared to the carrier power, we define the modulated electric field vector phasor by,

$$\begin{aligned}\tilde{\mathbf{E}}(\vec{r}, t) &= \mathbf{E}_p(\vec{r})e^{-j\omega_p t} \left( 1 + \frac{m_{\text{am}}}{2}(e^{-j\omega_a t} + e^{j\omega_a t}) \right. \\ &\quad \left. + \frac{m_{\text{pm}}}{2}(e^{j\omega_a t} - e^{-j\omega_a t}) \right) \\ &= \mathbf{E}_p(\vec{r})e^{-j\omega_p t} \left( 1 + \frac{m_{\text{am}} - m_{\text{pm}}}{2}e^{-j\omega_a t} \right. \\ &\quad \left. + \frac{m_{\text{am}} + m_{\text{pm}}}{2}e^{j\omega_a t} \right)\end{aligned}\quad (5)$$

and its complex conjugate by,

$$\begin{aligned}\tilde{\mathbf{E}}^*(\vec{r}, t) &= \mathbf{E}_p^*(\vec{r})e^{j\omega_p t} \left( 1 + \frac{m_{\text{am}} - m_{\text{pm}}}{2}e^{j\omega_a t} \right. \\ &\quad \left. + \frac{m_{\text{am}} + m_{\text{pm}}}{2}e^{-j\omega_a t} \right),\end{aligned}\quad (6)$$

where the AM and PM modulation indices,  $m_{\text{am}}$  and  $m_{\text{pm}}$ , are much less than unity, with the corresponding phasor diagram shown in Fig. 5. Likewise, the magnetic field and electric current vector phasors will have similar form. Next we take the time derivative of Eq. (5) and obtain,

$$\begin{aligned}\partial_t \tilde{\mathbf{E}}(\vec{r}, t) &\approx -j\omega_p \mathbf{E}_p(\vec{r})e^{-j\omega_p t} \left( 1 + \frac{m_{\text{am}} - m_{\text{pm}}}{2}e^{-j\omega_a t} \right. \\ &\quad \left. + \frac{m_{\text{am}} + m_{\text{pm}}}{2}e^{j\omega_a t} \right) \\ &\approx -j\omega_p \tilde{\mathbf{E}}(\vec{r}, t)\end{aligned}\quad (7)$$

and likewise

$$\partial_t \tilde{\mathbf{E}}^*(\vec{r}, t) \approx j\omega_p \tilde{\mathbf{E}}^*(\vec{r}, t) \quad (8)$$

in the limit where  $\omega_p \gg \omega_a$ , which allows us to ignore terms of order  $\sim \frac{m_{\text{am/pm}}\omega_a}{\omega_p}$ .

Thus, from Eq. (3), (7), and (8), the axion modified Ampere's law in phasor form may be shown to be,

$$\begin{aligned}\frac{1}{\mu_0} \nabla \times \tilde{\mathbf{B}} &= \tilde{\mathbf{J}}_e - j\omega_p \epsilon_0 \tilde{\mathbf{E}} + j\omega_a \epsilon_0 \tilde{\Theta} \tilde{\mathbf{B}} \\ \frac{1}{\mu_0} \nabla \times \tilde{\mathbf{B}}^* &= \tilde{\mathbf{J}}_e^* + j\omega_p \epsilon_0 \tilde{\mathbf{E}}^* - j\omega_a \epsilon_0 \tilde{\Theta}^* c \tilde{\mathbf{B}}^*\end{aligned}\quad (9)$$

while, the phasor form of the Faraday's law in (3) becomes,

$$\begin{aligned}\nabla \times \tilde{\mathbf{E}} &= j\omega_p \tilde{\mathbf{B}} \\ \nabla \times \tilde{\mathbf{E}}^* &= -j\omega_p \tilde{\mathbf{B}}^*,\end{aligned}\quad (10)$$

Next, we may implement Eqs. (9) and (10) to calculate the integral equations for the equivalent axion modified complex Poynting theorem.

#### IV. AXION UPCONVERSION SENSITIVITY FOR RESONANT MODES WITH NONZERO HELICITY

In this section we apply complex Poynting theorem from the phasor form developed in the last section, to calculate the sensitivity of the anyon cavity resonator to ultralight axions [68]. The complex Poynting vector and its complex conjugate are defined by,

$$\begin{aligned}\mathbf{S} &= \frac{1}{2\mu_0} \tilde{\mathbf{E}} \times \tilde{\mathbf{B}}^* \quad \text{and} \quad \mathbf{S}^* = \frac{1}{2\mu_0} \tilde{\mathbf{E}}^* \times \tilde{\mathbf{B}}, \\ \text{where } \text{Re}(\mathbf{S}) &= \frac{1}{2}(\mathbf{S} + \mathbf{S}^*).\end{aligned}\quad (11)$$

Here  $\mathbf{S}$  is the complex power density, with the real part,  $\text{Re}(\mathbf{S})$ , equal to the time averaged power density and the imaginary term equal to the reactive power, which will be zero at the frequency of a resonant mode as the inductive and capacitive terms cancel. Taking the divergence of  $\mathbf{S}$  in Eq. (11) we find,

$$\nabla \cdot \mathbf{S} = \frac{1}{2\mu_0} \tilde{\mathbf{B}}^* \cdot (\nabla \times \tilde{\mathbf{E}}) - \frac{1}{2\mu_0} \tilde{\mathbf{E}} \cdot (\nabla \times \tilde{\mathbf{B}}^*) \quad (12)$$

Combining (12) with (9), we obtain,

$$\begin{aligned}\nabla \cdot \mathbf{S} &= \frac{j\omega_p}{2} \left( \frac{1}{\mu_0} \tilde{\mathbf{B}}^* \cdot \tilde{\mathbf{B}} - \epsilon_0 \tilde{\mathbf{E}} \cdot \tilde{\mathbf{E}}^* \right) - \frac{1}{2} \tilde{\mathbf{E}} \cdot \tilde{\mathbf{J}}_e^* \\ &\quad + \frac{j\omega_a \epsilon_0 c}{2} \tilde{\mathbf{E}} \cdot \tilde{\Theta}^* \tilde{\mathbf{B}}^*\end{aligned}\quad (13)$$

Finally, by applying the divergence theorem and using (13) and the complex conjugate, we obtain,

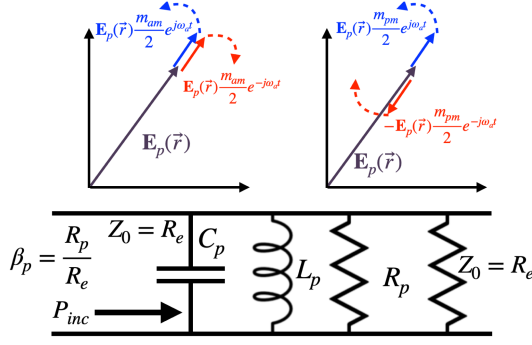


FIG. 5. Phasor diagram of  $\tilde{\mathbf{E}}(\vec{r}, t)$  with respect to the rotating frame  $e^{-j\omega_p t}$ . Top left; shows the amplitude modulated carrier. Top right; shows the frequency modulated carrier. The modulations are assumed to be single tone and small, ( $m_{am}, m_{fm} \ll 1$ ). The lower sideband is shown in red, while the upper sideband is shown in blue. Bottom; equivalent parallel LCR circuit model of a resonant mode with a coupling of  $\beta_p$ , when impedance matched  $\beta_p = 1$ .

$$\oint \text{Re}(\mathbf{S}) \cdot \hat{n} ds = \frac{j\omega_a \epsilon_0 c}{4} \int (\tilde{\mathbf{E}} \cdot \tilde{\mathbf{\Theta}}^* \tilde{\mathbf{B}}^* - \tilde{\mathbf{E}}^* \cdot \tilde{\mathbf{\Theta}} \tilde{\mathbf{B}} - \frac{1}{4} \int (\tilde{\mathbf{E}} \cdot \tilde{\mathbf{J}}_e^* + \tilde{\mathbf{E}}^* \cdot \tilde{\mathbf{J}}_e) d\tau, \quad (14)$$

which represents the relevant Poynting theorem equation to calculate the sensitivity to axions.

The integral on the left-hand side of (14) represents the incident carrier power delivered to the cavity equivalent (see Fig. 5) at the carrier frequency, so  $\oint \text{Re}(\mathbf{S}) \cdot \hat{n} ds = -\frac{4\beta_p P_{inc}}{(1+\beta_p)}$ , where  $P_{inc}$  is the incident power and  $\beta_p$  is the coupling, the negative sign is because the power is entering the resonator from an external source, rather than leaving. Note when the coupling is unity the resonator is impedance matched and  $\oint \text{Re}(\mathbf{S}) \cdot \hat{n} ds = -P_{inc}$ . Thus, starting with Eq. (14) we substitute the values of  $\tilde{\mathbf{J}}_e \approx \frac{\omega_p \epsilon_0}{Q_p} \tilde{\mathbf{E}}$  and  $\tilde{\mathbf{J}}_e^* \approx \frac{\omega_p \epsilon_0}{Q_p} \tilde{\mathbf{E}}^*$ , to obtain,

$$-P_{inc} \frac{4\beta_p}{(1+\beta_p)} = \frac{j\omega_a \epsilon_0 c}{4} \int (\tilde{\mathbf{E}} \cdot \tilde{\mathbf{\Theta}}^* \tilde{\mathbf{B}}^* - \tilde{\mathbf{E}}^* \cdot \tilde{\mathbf{\Theta}} \tilde{\mathbf{B}} - \frac{\omega_p \epsilon_0}{Q_p} \frac{1}{2} \int \tilde{\mathbf{E}} \cdot \tilde{\mathbf{E}}^* d\tau. \quad (15)$$

Next we substitute the values of  $\tilde{\mathbf{E}}(\vec{r}, t)$ ,  $\tilde{\mathbf{B}}(\vec{r}, t)$ , and  $\tilde{\mathbf{\Theta}}(t)$ . To first order in the modulation side bands, we find

$$\tilde{\mathbf{E}}(\vec{r}, t) \cdot \tilde{\mathbf{E}}^*(\vec{r}, t) = \mathbf{E}_p(\vec{r}) \cdot \mathbf{E}_p^*(\vec{r}) (1 + m_{am}(e^{-j\omega_a t} + e^{j\omega_a t})), \quad (16)$$

which only depends on amplitude modulation, as the phase sidebands are second order. Next, to leading at the same modulation frequency we find that,

$$\begin{aligned} & \tilde{\mathbf{E}}(\vec{r}, t) \cdot \tilde{\mathbf{\Theta}}^*(t) \tilde{\mathbf{B}}^*(\vec{r}, t) - \tilde{\mathbf{E}}^*(\vec{r}, t) \cdot \tilde{\mathbf{\Theta}}(t) \tilde{\mathbf{B}}(\vec{r}, t) \\ &= \mathbf{E}_p(\vec{r}) \cdot \mathbf{B}_p^*(\vec{r}) \theta_0 e^{j\omega_a t} - \mathbf{E}_p^*(\vec{r}) \cdot \mathbf{B}_p(\vec{r}) \theta_0 e^{-j\omega_a t} \\ &= j\text{Im}[\mathbf{E}_p(\vec{r}) \cdot \mathbf{B}_p^*(\vec{r})] \theta_0 (e^{j\omega_a t} + e^{-j\omega_a t}). \end{aligned} \quad (17)$$

Substituting (16) and (17) into (15) gives two equations, one at the carrier frequency and one at the modulation side bands.

At the carrier frequency the stored electromagnetic energy in the resonator mode is known to be,

$$U_p = \frac{\epsilon_0}{2} \int \mathbf{E}_p(\vec{r}) \cdot \mathbf{E}_p^*(\vec{r}) d\tau, \quad (18)$$

so we obtain the following equation, which represents the dissipated power,  $P_d$  in the steady state,

$$P_d = \frac{\omega_p U_p}{Q_p} = \frac{4\beta_p}{(1+\beta_p)} P_{inc}. \quad (19)$$

The fraction of the dissipated power in the coupling resistor  $R_e$  is then given by,

$$P_p = \frac{\beta_p P_d}{\beta_p + 1} = \frac{4\beta_p^2}{(1+\beta_p)^2} P_{inc}. \quad (20)$$

At the modulation sideband frequency the following value of the AM modulation index may be determined,

$$m_{am} = -\frac{\langle \theta_0 \rangle Q_p \omega_a \text{Im}[\int \mathbf{E}_p(\vec{r}) \cdot \mathbf{B}_p^*(\vec{r}) d\tau]}{\omega_p \sqrt{2 \int \mathbf{E}_p(\vec{r}) \cdot \mathbf{E}_p^*(\vec{r}) d\tau \int \mathbf{B}_p(\vec{r}) \cdot \mathbf{B}_p^*(\vec{r}) d\tau}}, \quad (21)$$

which in terms of helicity given by Eq. (1), becomes,

$$|m_{am}| = \frac{1}{2\sqrt{2}} Q_p \frac{\omega_a}{\omega_p} \langle \theta_0 \rangle |\mathcal{H}_p|, \quad (22)$$

proportional to the normalized mode helicity of a monochromatic field [51–58]. Thus, the fraction of the power in the amplitude modulated sidebands is given by,

$$P_{am} = m_{am}^2 P_p = Q_p^2 \frac{4\beta_p^2}{(1+\beta_p)^2} \left( \frac{\omega_a}{\omega_p} \right)^2 \frac{\langle \theta_0 \rangle^2}{8} \mathcal{H}_p^2 P_{inc}. \quad (23)$$

Here,  $\mathcal{H}_p^2$  is analogous to a DC haloscope form factor [65]. The above calculation assumes that the axion frequency is within the bandwidth of the resonant mode, which will be true in the ultralight regime. In general we must substitute  $Q_p \rightarrow \frac{Q_p}{\sqrt{1+4Q_p^2(\frac{\omega_a}{\omega_p})^2}}$  to take into account the cavity resonator bandwidth.

In actual fact the axion presents as a narrowband signal oscillating at the axion frequency,  $f_a = \frac{\omega_a}{2\pi}$ , virtualized as a

Maxwell-Boltzmann distribution of about a part in  $10^6$ , equivalent to a narrowband noise source with a frequency spread of  $10^{-6}f_a$  Hz. Defining the spectral density of the axion field as,  $S_A(f)$  [kg/s/Hz], from (23) the axion induced AM spectral density,  $S_{A_{\text{am}}}$ , is given by,

$$S_{A_{\text{am}}}(f) = g_{a\gamma\gamma}^2 \frac{\beta_p^2}{2(1+\beta_p)^2} \frac{Q_p^2}{1+4Q_p^2(\frac{f_a}{f_p})^2} \left(\frac{f_a}{f_p}\right)^2 \mathcal{H}_p^2 S_A(f), \quad (24)$$

To calculate the signal to noise ratio we need to relate the axion angle,  $\theta_0$ , to the dark matter density at the earth,  $\rho_a$ , where the cold dark matter density is taken to be  $\rho_a = 8 \times 10^{-22}$  kg/m<sup>3</sup> (i.e., 0.45 GeV/cm<sup>3</sup>) in this analysis. This may be done in the standard way, where  $\langle\theta_0\rangle^2 = g_{a\gamma\gamma}^2 \langle a_0 \rangle^2 = g_{a\gamma\gamma}^2 \frac{\rho_a}{c} \frac{\hbar^2}{m_a^2} = g_{a\gamma\gamma}^2 \rho_a \frac{c^3}{\omega_a^2}$ . Thus integrating over the bandwidth of (24) and given the pump oscillator has an amplitude noise spectral density of  $S_{\text{am}}$  per Hz, the signal to noise ratio is given by,

$$SNR = \frac{g_{a\gamma\gamma} \beta_p |\mathcal{H}_p|}{\sqrt{2}(1+\beta_p)} \frac{Q_p}{\sqrt{1+4Q_p^2(\frac{\omega_a}{\omega_p})^2}} \frac{(\frac{10^6}{f_a})^{\frac{1}{4}} \sqrt{\rho_a c^3}}{\omega_p \sqrt{S_{\text{am}}}}. \quad (25)$$

This assumes the measurement time,  $t$  is greater than the axion coherence time so that  $t > \frac{10^6}{f_a}$ . For measurement times of  $t < \frac{10^6}{f_a}$  we substitute  $(\frac{10^6}{f_a})^{\frac{1}{4}} \rightarrow t^{\frac{1}{4}}$ . Note, there will be a frequency modulation as well. However, this will be proportional to the real part of Eqn. (1), so the sensitivity will be reduced by a factor of  $Q_p$  with a SNR independent of  $Q_p$ , while the amplitude modulations are directly proportional to  $Q_p$ .

### A. Sensitivity to axions in quantum electromagnetodynamics

Recently it was shown that there is a further modification of axion electrodynamics through the existence of putative magnetically charged matter [69,70], and assuming  $\nabla a = 0$ , the modified Ampere's and Faraday's law may be written in phasor amplitude form as [71,72],

$$\begin{aligned} \frac{1}{\mu_0} \nabla \times \tilde{\mathbf{B}} &= \tilde{\mathbf{J}}_e - j\omega_p \epsilon_0 \tilde{\mathbf{E}} + j\omega_a \epsilon_0 c g_{a\gamma\gamma} \tilde{\mathbf{B}} - j\omega_a \epsilon_0 g_{aEM} \tilde{\mathbf{a}} \tilde{\mathbf{E}} \\ \text{and } \nabla \times \tilde{\mathbf{E}} &= j\omega_p \tilde{\mathbf{B}} + j \frac{\omega_a g_{aMM}}{c} \tilde{\mathbf{a}} \tilde{\mathbf{E}} - j\omega_a g_{aEM} \tilde{\mathbf{a}} \tilde{\mathbf{B}}, \end{aligned} \quad (26)$$

respectively, where  $g_{aEM}$  and  $g_{aMM}$  are extra axion-photon coupling term if high energy magnetic charge exists. Then from Poynting theorem and with some algebra it is straight

forward to show that Eq. (14) is of the same form, but with  $\theta_0 = (g_{a\gamma\gamma} + g_{aMM})a_0$ . Thus, limits on  $g_{a\gamma\gamma}$  presented in this work is equivalent to limits on  $g_{a\gamma\gamma} + g_{aMM}$ , allowing a unique sensitive search for ultra-light axions in the mass range  $10^{-22}$  to  $10^{-14}$  using only a single mode without the need for dual-mode excitation or a large volume magnet.

## V. POSSIBLE EXPERIMENTAL CONFIGURATIONS AND SENSITIVITY

The previously studied dual-mode upconversion experiment excites two modes in one cavity, with a pump mode and a readout mode [50], where the pump mode acts as a background field, which interacts with the putative axion dark matter background to generate photons or frequency perturbations at the readout mode frequency. This experiment is similar, except only the implementation of a single mode is necessary because the mode acts as its own background field and thus in the upconversion limit is sensitive to ultra light dark matter axions. The best way to configure such upconversion experiments is as a frequency stabilized oscillator locked tightly to the axion sensitive cavity as shown in Fig. 6, here we propose two possible configurations similar to what was experimentally considered in [50], except without the complication of the extra pump mode. A variety of phase detection techniques are possible for both configurations, including the use of

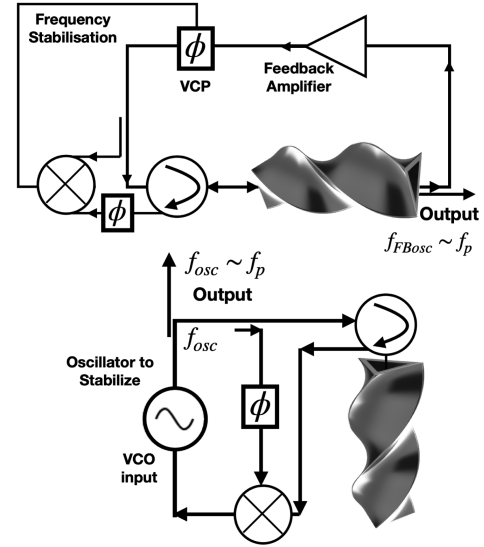


FIG. 6. Top, Schematic of a frequency stabilized loop oscillator configuration using a phase detector (mixer) to frequency lock the feed back oscillation,  $f_{FBosc}$  to the anyon cavity resonant frequency,  $f_p$ , via a voltage controlled phase shifter (VCP). Bottom, schematic of an external voltage controlled oscillator (VCO) frequency locked to the anyon cavity resonator, using a phase detector (mixer), so  $f_{osc} \sim f_p$ . In both cases the resonator and phase detector combine to make a frequency discriminator, which sets the oscillator frequency lock equal to the frequency of the anyon cavity resonator.

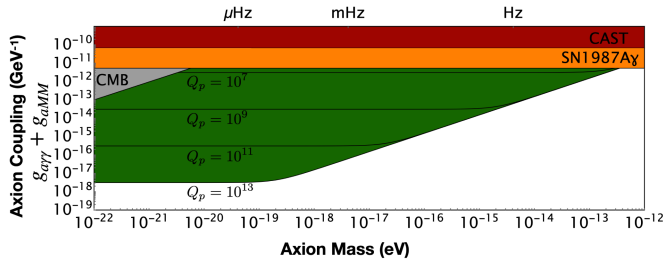


FIG. 7. Predicted exclusion regions of axion-photon coupling strength  $g_{a\gamma\gamma} + g_{aMM}$  of a low-mass axion search conducted by an anyon cavity with different  $Q_p$  values for a 1.3 GHz cavity (green), as well as limits set by astrophysical observations. With current 3D printed aluminium technology  $Q_p = 10^7$  [27] is possible, with the plausible limits also set by the best superconducting technology [28–30].

interferometric [73–76] and Pound modulated systems [77] to significantly reduce the oscillator phase noise. To calculate the phase noise in oscillators commonly one considers the Lesson effect, which degrades the close to the carrier phase noise. However, it has been shown that the equivalent Leeson effect is much smaller for amplitude noise [78]. Thus, this experiment gains at low Fourier frequencies as the amplitude noise fluctuations are much smaller in this regime, with better than  $S_{am} = -160$  dBc/Hz possible at low Fourier frequency offsets. Usually one can lock the oscillator to one in parts of  $10^7$  of the line width. For such oscillators there will be essentially no measurable frequency-to-amplitude noise conversions. To optimize the sensitivity to axions, ways to reduce the oscillator amplitude noise must be implemented, which are compatible with the frequency stabilization techniques.

The estimates of possible sensitivities are detailed in Fig. 7. These sensitivities are attained by solving equation (25) for  $g_{a\gamma\gamma}$  as a function of axion frequency  $f_a = \omega_a/2\pi$ , setting  $SNR = 1$ , assuming critical mode coupling  $\beta_p = 1$ ,  $|\mathcal{H}_p| = 1$ ,  $\omega_p/2\pi = 1$  GHz, the cold dark matter density  $\rho_a = 8 \times 10^{-22}$  kg/m<sup>3</sup> (i.e., 0.45 GeV/cm<sup>3</sup>),  $c$  the speed of light and the spectral density of the oscillator amplitude fluctuations is assumed to be  $-160$  dBc/Hz [78]. Sensitivities for different values of cavity  $Q$ -factor  $Q_p$  are shown over the range discussed in the text. In actual fact, if we consider the full quantum electromagnetodynamic modifications to electrodynamics [69,70], the

experiment will put a limit on  $g_{a\gamma\gamma} + g_{aMM}$  [71,72], which we show in Fig. 7.

This calculation does not include systematics, which with careful design of the oscillator should be able to be eliminated, the experimental research program will include identifying these effects, such as temperature, pressure, vibration, and magnetic sensitivities. This approach has been undertaken previously using oscillators for other tests of fundamental physics, such as tests for Lorentz invariance violation, Local position invariance and tests on fundamental constants, with continuous oscillator measurements over multiple years [79–81]. Thus with careful design and measurement we believe there is high probability of attaining these fundamental limits, which will mainly depend on the achievable value of cavity  $Q$ -factor. Other ways to experimentally increase the signal to noise ratio are possible, including constructing multiple arrays of oscillators and the use of cross-correlation techniques [82], in general, resonant frequencies should be close, but would not need to be tuned to the same frequencies when using modern noise measurement systems.

## VI. CONCLUSIONS

It has been demonstrated that an electromagnetic field with nonzero helicity,  $\mathcal{H}_p$  will be sensitive to ULDM axions. This unique property in an electromagnetic resonator is achievable using hollow, twisted triangular devices in either a linear or ring configuration. FEM has demonstrated that the eigenmodes of such systems do indeed produce  $|\mathcal{H}_p| \sim 1$  for particular modes, and that these modes in fact tune in frequency as a function of twist angle  $\phi$ . Three discrete  $\phi$  valued linear resonators are 3D printed and demonstrate excellent agreement with predicted mode frequencies. If theoretically achievable  $Q$ -factors are attained, an ultrastable oscillator based off one of these anyon cavity devices would permit the world's most sensitive search for axion dark matter in the ultralight mass range.

## ACKNOWLEDGMENTS

This work was funded by the Australian Research Council Centre of Excellence for Engineered Quantum Systems, CE170100009 and the Centre of Excellence for Dark Matter Particle Physics, CE200100008.

- [1] Julian Schwinger, On gauge invariance and vacuum polarization, *Phys. Rev.* **82**, 664 (1951).
- [2] Stephen L. Adler, Axial-vector vertex in spinor electrodynamics, *Phys. Rev.* **177**, 2426 (1969).

- [3] Johannes Gooth, Anna C. Niemann, Tobias Meng, Adolfo G. Grushin, Karl Landsteiner, Bernd Gotsmann, Fabian Menges, Marcus Schmidt, Chandra Shekhar, Vicky SuB, Ruben Huhne, Bernd Rellinghaus, Claudia Felser, Binghai



- Yan, and Kornelius Nielsch, Experimental signatures of the mixed axial-gravitational anomaly in the Weyl semimetal NbP, *Nature (London)* **547**, 324 (2017).
- [4] Zejian Ren, Dong Liu, Entong Zhao, Chengdong He, Ka Kwan Pak, Jensen Li, and Gyu-Boong Jo, Chiral control of quantum states in non-Hermitian spin-orbit-coupled fermions, *Nat. Phys.* **18**, 385 (2022).
- [5] Dung Vu, Wenjuan Zhang, Cuneyt Sahin, Michael E. Flatte, Nandini Trivedi, and Joseph P. Heremans, Thermal chiral anomaly in the magnetic-field-induced ideal Weyl phase of Bi<sub>1-x</sub>Sb<sub>x</sub>, *Nat. Mater.* **20**, 1525 (2021).
- [6] J. Gooth, B. Bradlyn, S. Honnali, C. Schindler, N. Kumar, J. Noky, Y. Qi, C. Shekhar, Y. Sun, Z. Wang, B. A. Bernevig, and C. Felser, Axionic charge-density wave in the Weyl semimetal (TaSe<sub>4</sub>)<sub>2</sub>I, *Nature (London)* **575**, 315 (2019).
- [7] D. I. Pikulin, Anffany Chen, and M. Franz, Chiral Anomaly from Strain-Induced Gauge Fields in Dirac and Weyl Semimetals, *Phys. Rev. X* **6**, 041021 (2016).
- [8] Zhong Wang and Shou-Cheng Zhang, Chiral anomaly, charge density waves, and axion strings from Weyl semimetals, *Phys. Rev. B* **87**, 161107 (2013).
- [9] Benjamin J. Wieder, Barry Bradlyn, Jennifer Cano, Zhijun Wang, Maia G. Vergniory, Luis Elcoro, Alexey A. Soluyanov, Claudia Felser, Titus Neupert, Nicolas Regnault, and B. Andrei Bernevig, Topological materials discovery from crystal symmetry, *Nat. Rev. Mater.* **7**, 196 (2022).
- [10] Vladimir M. Fomin, Roman O. Rezaev, and Oleksandr V. Dobrovolskiy, Topological transitions in ac/dc-driven superconductor nanotubes, *Sci. Rep.* **12**, 10069 (2022).
- [11] Lewis E. MacKenzie and Patrycja Stachelek, The twists and turns of chiral chemistry, *Nat. Chem.* **13**, 521 (2021).
- [12] Yiqiao Tang and Adam E. Cohen, Enhanced enantioselectivity in excitation of chiral molecules by superchiral light, *Science* **332**, 333 (2011).
- [13] Luisa Torsi, Gianluca M. Farinola, Francesco Marinelli, M. Cristina Tanese, Omar Hassan Omar, Ludovico Valli, Francesco Babudri, Francesco Palmisano, P. Giorgio Zambonin, and Francesco Naso, A sensitivity-enhanced field-effect chiral sensor, *Nat. Mater.* **7**, 412 (2008).
- [14] E. Hendry, T. Carpy, J. Johnston, M. Popland, R. V. Mikhaylovskiy, A. J. Laphorn, S. M. Kelly, L. D. Barron, N. Gadegaard, and M. Kadodwala, Ultrasensitive detection and characterization of biomolecules using superchiral fields, *Nat. Nanotechnol.* **5**, 783 (2010).
- [15] Yiqiao Tang and Adam E. Cohen, Optical Chirality and its Interaction with Matter, *Phys. Rev. Lett.* **104**, 163901 (2010).
- [16] Jungho Mun, Minkyung Kim, Younghwan Yang, Trevon Badloe, Jincheng Ni, Yang Chen, Cheng-Wei Qiu, and Junsuk Rho, Electromagnetic chirality: From fundamentals to nontraditional chiroptical phenomena, *Light* **9**, 139 (2020).
- [17] Mingkai Liu, David A. Powell, Ilya V. Shadrivov, Mikhail Lapine, and Yuri S. Kivshar, Spontaneous chiral symmetry breaking in metamaterials, *Nat. Commun.* **5**, 4441 (2014).
- [18] Alexander B. Khanikaev, S. Hossein Mousavi, Wang-Kong Tse, Mehdi Kargarian, Allan H. MacDonald, and Gennady Shvets, Photonic topological insulators, *Nat. Mater.* **12**, 233 (2013).
- [19] Maxim Goryachev and Michael E. Tobar, Reconfigurable Microwave Photonic Topological Insulator, *Phys. Rev. Appl.* **6**, 064006 (2016).
- [20] Biao Yang, Mark Lawrence, Wenlong Gao, Qinghua Guo, and Shuang Zhang, One-way helical electromagnetic wave propagation supported by magnetized plasma, *Sci. Rep.* **6**, 21461 (2016).
- [21] Xuanru Zhang and Tie Jun Cui, Single-particle dichroism using orbital angular momentum in a microwave plasmonic resonator, *ACS Photonics* **7**, 3291 (2020).
- [22] Douglas J. Ballon and Henning U. Voss, Classical Möbius-Ring Resonators Exhibit Fermion-Boson Rotational Symmetry, *Phys. Rev. Lett.* **101**, 247701 (2008).
- [23] Renée Hložek, David J. E. Marsh, Daniel Grin, Rupert Allison, Jo Dunkley, and Erminia Calabrese, Future cmb tests of dark matter: Ultralight axions and massive neutrinos, *Phys. Rev. D* **95**, 123511 (2017).
- [24] Alberto Diez-Tejedor and David J. E. Marsh, Cosmological production of ultralight dark matter axions, *arXiv:1702.02116*.
- [25] Jiajun Zhang, Yue-Lin Sming Tsai, Jui-Lin Kuo, Kingman Cheung, and Ming-Chung Chu, Ultralight axion dark matter and its impact on dark halo structure in n-body simulations, *Astrophys. J.* **853**, 51 (2018).
- [26] Michael A. Fedderke, Peter W. Graham, and Surjeet Rajendran, Axion dark matter detection with CMB polarization, *Phys. Rev. D* **100**, 015040 (2019).
- [27] Daniel L. Creedon, Maxim Goryachev, Nikita Kostylev, Timothy B. Sercombe, and Michael E. Tobar, A 3d printed superconducting aluminium microwave cavity, *Appl. Phys. Lett.* **109**, 032601 (2016).
- [28] A. Romanenko, R. Pilipenko, S. Zorzetti, D. Frolov, M. Awida, S. Belomestnykh, S. Posen, and A. Grassellino, Three-Dimensional Superconducting Resonators at  $t = 20$  mK with Photon Lifetimes up to  $\tau = 2$  s, *Phys. Rev. Appl.* **13**, 034032 (2020).
- [29] S. Posen, A. Romanenko, A. Grassellino, O. S. Melnychuk, and D. A. Sergatskov, Ultralow Surface Resistance via Vacuum Heat Treatment of Superconducting Radio-Frequency Cavities, *Phys. Rev. Appl.* **13**, 014024 (2020).
- [30] Ben T. McAllister, Jeremy Bourhill, Wing Him Jacob Ma, Tim Sercombe, Maxim Goryachev, and Michael E. Tobar, Characterization of cryogenic material properties of 3-d-printed superconducting niobium using a 3-d lumped element microwave cavity, *IEEE Trans. Instrum. Meas.* **70**, 1 (2021).
- [31] R. D. Peccei and Helen R. Quinn, CP Conservation in the Presence of Pseudoparticles, *Phys. Rev. Lett.* **38**, 1440 (1977).
- [32] R. D. Peccei and Helen R. Quinn, Constraints imposed by CP conservation in the presence of pseudoparticles, *Phys. Rev. D* **16**, 1791 (1977).
- [33] Steven Weinberg, A New Light Boson?, *Phys. Rev. Lett.* **40**, 223 (1978).
- [34] F. Wilczek, Problem of Strong  $p$  and  $t$  Invariance in the Presence of Instantons, *Phys. Rev. Lett.* **40**, 279 (1978).
- [35] Luca Di Luzio, Belen Gavela, Pablo Quilez, and Andreas Ringwald, An even lighter QCD axion, *J. High Energy Phys.* **05** (2021) 184.

- [36] Luca Di Luzio, Belen Gavela, Pablo Quilez, and Andreas Ringwald, Dark matter from an even lighter QCD axion: Trapped misalignment, *J. Cosmol. Astropart. Phys.* **10** (2021) 001.
- [37] Anton V. Sokolov and Andreas Ringwald, Photophilic hadronic axion from heavy magnetic monopoles, *J. High Energy Phys.* **06** (2021) 123.
- [38] Luca Visinelli and Sunny Vagnozzi, Cosmological window onto the string axiverse and the supersymmetry breaking scale, *Phys. Rev. D* **99**, 063517 (2019).
- [39] Teng Wu, John W. Blanchard, Gary P. Centers, Nataniel L. Figueroa, Antoine Garcon, Peter W. Graham, Derek F. Jackson Kimball, Surjeet Rajendran, Yevgeny V. Stadnik, Alexander O. Sushkov, Arne Wickenbrock, and Dmitry Budker, Search for Axionlike Dark Matter with a Liquid-State Nuclear Spin Comagnetometer, *Phys. Rev. Lett.* **122**, 191302 (2019).
- [40] Tanya S. Roussy, Daniel A. Palken, William B. Cairncross, Benjamin M. Brubaker, Daniel N. Gresh, Matt Grau, Kevin C. Cossel, Kia Boon Ng, Yuval Shagam, Yan Zhou, Victor V. Flambaum, Konrad W. Lehnert, Jun Ye, and Eric A. Cornell, Experimental Constraint on Axionlike Particles Over Seven Orders of Magnitude in Mass, *Phys. Rev. Lett.* **126**, 171301 (2021).
- [41] Min Jiang, Haowen Su, Antoine Garcon, Xinhua Peng, and Dmitry Budker, Search for axion-like dark matter with spin-based amplifiers, *Nat. Phys.* **17**, 1402 (2021).
- [42] Itay M. Bloch, Gil Ronen, Roy Shaham, Ori Katz, Tomer Volansky, and Or Katz, New constraints on axion-like dark matter using a floquet quantum detector, *Sci. Adv.* **8**, eabl8919 (2022).
- [43] Maxim Goryachev, Ben T. McAllister, and Michael E. Tobar, Axion detection with precision frequency metrology, *Phys. Dark Universe* **26**, 100345 (2019).
- [44] Catriona Thomson, Maxim Goryachev, Ben T. McAllister, and Michael E. Tobar, Corrigendum to “axion detection with precision frequency metrology” [Phys. Dark Universe 26 (2019) 100345], *Phys. Dark Universe* **32**, 100787 (2021).
- [45] Robert Lasenby, Microwave cavity searches for low-frequency axion dark matter, *Phys. Rev. D* **102**, 015008 (2020).
- [46] Robert Lasenby, Parametrics of electromagnetic searches for axion dark matter, *Phys. Rev. D* **103**, 075007 (2021).
- [47] Asher Berlin, Raffaele Tito D’Agnolo, Sebastian A. R. Ellis, Christopher Nantista, Jeffrey Neilson, Philip Schuster, Sami Tantawi, Natalia Toro, and Kevin Zhou, Axion dark matter detection by superconducting resonant frequency conversion, *J. High Energy Phys.* **07** (2020) 001.
- [48] Catriona A. Thomson, Ben T. McAllister, Maxim Goryachev, Eugene N. Ivanov, and Michael E. Tobar, Upconversion Loop Oscillator Axion Detection Experiment: A Precision Frequency Interferometric Axion Dark Matter Search with a Cylindrical Microwave Cavity, *Phys. Rev. Lett.* **126**, 081803 (2021); **127**, 019901(E) (2021).
- [49] Asher Berlin, Raffaele Tito D’Agnolo, Sebastian A. R. Ellis, and Kevin Zhou, Heterodyne broadband detection of axion dark matter, *Phys. Rev. D* **104**, L111701 (2021).
- [50] Catriona A. Thomson, Maxim Goryachev, Ben T. McAllister, Eugene N. Ivanov, Paul Altin, and Michael E. Tobar, Searching for low-mass axions using resonant upconversion, *Phys. Rev. D* **107**, 112003 (2023).
- [51] Robert P. Cameron and Stephen M. Barnett, Electric-magnetic symmetry and Noether’s theorem, *New J. Phys.* **14**, 123019 (2012).
- [52] Robert P. Cameron, Stephen M. Barnett, and Alison M. Yao, Optical helicity, optical spin and related quantities in electromagnetic theory, *New J. Phys.* **14**, 053050 (2012).
- [53] Konstantin Y. Bliokh, Aleksandr Y. Bekshaev, and Franco Nori, Dual electromagnetism: Helicity, spin, momentum and angular momentum, *New J. Phys.* **15**, 033026 (2013).
- [54] Konstantin Y. Bliokh, Yuri S. Kivshar, and Franco Nori, Magnetoelectric Effects in Local Light-Matter Interactions, *Phys. Rev. Lett.* **113**, 033601 (2014).
- [55] Konstantin Y. Bliokh, Aleksandr Y. Bekshaev, and Franco Nori, Corrigendum: Dual electromagnetism: Helicity, spin, momentum, and angular momentum (2013new j. phys.15033026), *New J. Phys.* **18**, 089503 (2016).
- [56] Konstantin Y. Bliokh and Franco Nori, Transverse and longitudinal angular momenta of light, *Phys. Rep.* **592**, 1 (2015).
- [57] F. Alpeggiani, K. Y. Bliokh, F. Nori, and L. Kuipers, Electromagnetic Helicity in Complex Media, *Phys. Rev. Lett.* **120**, 243605 (2018).
- [58] Lei Wei and Francisco J. Rodríguez-Fortuño, Momentum-Space Geometric Structure of Helical Evanescent Waves and its Implications on Near-Field Directionality, *Phys. Rev. Appl.* **13**, 014008 (2020).
- [59] Daniel M. Lipkin, Existence of a new conservation law in electromagnetic theory, *J. Math. Phys. (N.Y.)* **5**, 696 (1964).
- [60] R. D. Peccei, The strong *CP* problem and axions, *Lect. Notes Phys.* **741**, 3 (2008).
- [61] Christophe Caloz and Ari Sihvola, Electromagnetic chirality, part 1: The microscopic perspective [electromagnetic perspectives], *IEEE Antennas Propag. Mag.* **62**, 58 (2020).
- [62] J. Krupka, M. E. Tobar, J. G. Hartnett, D. Cros, and J.-M. Le Floch, Extremely high-q factor dielectric resonators for millimeter-wave applications, *IEEE Trans. Microwave Theory Tech.* **53**, 702 (2005).
- [63] Ana Morán-López, Jorge A. Ruiz-Cruz, Juan Córcoles, José R. Montejo-Garai, and Jesús M. Rebollar, Analytical expressions of the q-factor for the complete resonant mode spectrum of the equilateral triangular waveguide cavity, *Electron. Lett.* **55**, 944 (2019).
- [64] Remi Léandre, Ana Morán-López, Juan Córcoles, Jorge A. Ruiz-Cruz, José R. Montejo-Garai, and Jesús M. Rebollar, Electromagnetic scattering at the waveguide step between equilateral triangular waveguides, *Adv. Theor. Math. Phys.* **2016**, 2974675 (2016).
- [65] Pierre Sikivie, Invisible axion search methods, *Rev. Mod. Phys.* **93**, 015004 (2021).
- [66] P. Sikivie, On the interaction of magnetic monopoles with axionic domain walls, *Phys. Lett.* **137B**, 353 (1984).
- [67] Frank Wilczek, Two Applications of Axion Electrodynamics, *Phys. Rev. Lett.* **58**, 1799 (1987).
- [68] Michael E. Tobar, Ben T. McAllister, and Maxim Goryachev, Poynting vector controversy in axion modified

- electrodynamics, *Phys. Rev. D* **105**, 045009 (2022); **106**, 109903(E) (2022).
- [69] Anton V. Sokolov and Andreas Ringwald, Electromagnetic couplings of axions, [arXiv:2205.02605](#).
- [70] Anton V. Sokolov and Andreas Ringwald, Generic axion Maxwell equations: Path integral approach, [arXiv:2303.10170](#).
- [71] Michael E. Tobar, Catriona A. Thomson, Benjamin T. McAllister, Maxim Goryachev, Anton V. Sokolov, and Andreas Ringwald, Sensitivity of resonant axion haloscopes to quantum electrodynamics, *Ann. Phys. (Berlin)* **2200594** (2023). [10.1002/andp.202200594](#)
- [72] Michael E. Tobar, Anton V. Sokolov, Andreas Ringwald, and Maxim Goryachev, Searching for gut-scale QCD axions and monopoles with a high voltage capacitor, *Phys. Rev. D* **108**, 035024 (2023).
- [73] Eugene N. Ivanov and Michael E. Tobar, Microwave phase detection at the level  $10^{-11}$ , *Rev. Sci. Instrum.* **80**, 044701 (2009).
- [74] E. N. Ivanov and M. E. Tobar, Low phase-noise microwave oscillators with interferometric signal processing, *IEEE Trans. Microwave Theory Tech.* **54**, 3284 (2006).
- [75] E. N. Ivanov and M. E. Tobar, Low phase-noise sapphire crystal microwave oscillators: Current status, *IEEE Trans. Ultrason. Ferroelectr. Freq. Control* **56**, 263 (2009).
- [76] E. N. Ivanov, M. E. Tobar, and R. A. Woode, Microwave interferometry: Application to precision measurements and noise reduction techniques, *IEEE Trans. Ultrason. Ferroelectr. Freq. Control* **45**, 1526 (1998).
- [77] C. R. Locke, E. N. Ivanov, J. G. Hartnett, P. L. Stanwix, and M. E. Tobar, Invited article: Design techniques and noise properties of ultrastable cryogenically cooled sapphire-dielectric resonator oscillators, *Rev. Sci. Instrum.* **79**, 051301 (2008).
- [78] E. Rubiola and R. Brendel, The am noise mechanism in oscillators, *IEEE IFCS Conf. Proc.* **33** (2009).
- [79] Moritz Nagel, Stephen R. Parker, Evgeny V. Kovalchuk, Paul L. Stanwix, John G. Hartnett, Eugene N. Ivanov, Achim Peters, and Michael E. Tobar, Direct terrestrial test of Lorentz symmetry in electrodynamics to  $10^{-18}$ , *Nat. Commun.* **6**, 8174 (2015).
- [80] M. E. Tobar, P. L. Stanwix, J. J. McFerran, J. Guena, M. Abgrall, S. Bize, A. Clairon, Ph. Laurent, P. Rosenbusch, D. Rovera, and G. Santarelli, Testing local position and fundamental constant invariance due to periodic gravitational and boost using long-term comparison of the SYRTE atomic fountains and h-masers, *Phys. Rev. D* **87**, 122004 (2013).
- [81] Michael Edmund Tobar, Peter Wolf, Sebastien Bize, Giorgio Santarelli, and Victor Flambaum, Testing local Lorentz and position invariance and variation of fundamental constants by searching the derivative of the comparison frequency between a cryogenic sapphire oscillator and hydrogen maser, *Phys. Rev. D* **81**, 022003 (2010).
- [82] Ben T. Mcallister, Stephen R. Parker, Eugene N. Ivanov, and Michael E. Tobar, Cross-correlation signal processing for axion and WISP dark matter searches, *IEEE Trans. Ultrason. Ferroelectr. Freq. Control* **66**, 236 (2019).